

Gazing at crystal balls - Electron backscatter diffraction indexing and cross correlation on a sphere

Ralf Hielscher^{a,*}, Felix Bartel^a, Thomas Benjamin Britton^b

^a*Fakultät für Mathematik, Technische Universität Chemnitz, 09107, Chemnitz, Germany*

^b*Department of Materials, Imperial College London, London, SW7 2AZ, UK*

Abstract

We present spherical analysis of electron backscatter diffraction (EBSD) patterns with two new algorithms: (1) pattern indexing utilising a spherical Radon transform and band localisation; (2) pattern indexing with spherical cross correlation on the surface of the sphere, with refinement. These new approaches are formally introduced and their accuracies are determined using dynamically simulated patterns. We demonstrate their utility with an experimental dataset obtained from ferritic iron. Our results indicate that analysis of EBSD patterns on the surface of a sphere provides a valuable method of unlocking information from these rich sources of crystallographic data.

Keywords: *Electron diffraction; electron microscopy; geometrical projection; cross correlation; crystallography*

Highlights

1. We present a method to approximate Kikuchi patterns on the surface of the sphere.
2. Our approximations enable spherical Radon transformations for pattern indexing.
3. Cross correlation is performed on the sphere for precise orientation determination.
4. All methods are speed optimised using fast Fourier algorithms on the sphere and the orientation space.

*Corresponding author

Email addresses: ralf.hielscher@mathematik.tu-chemnitz.de (Ralf Hielscher), b.britton@imperial.ac.uk (Thomas Benjamin Britton)

1. Introduction

Electron backscatter diffraction (EBSD) is a popular microscopy technique used to reveal crystallographic information about materials. Automated, quantitative, robust, and precise interpretation of each electron backscatter pattern (EBSP) (aka Kikuchi pattern) has long been a major advantage of the technique [1], especially when compared to other methods, such as transmission electron microscopy (TEM) imaging and until recently [2] with S(canning)TEM based mapping. To advance the EBSD technique further, it is advantageous to improve the quality of the information captured and simultaneously improve how we interpret each pattern. The latter motivates our present work, where we develop the spherical projection formally to formulate a spherical Radon transform and a spherical cross correlation. These two algorithms enable us to index each EBSD pattern automatically (using open source tools) and generate rich microstructure maps.

The majority of existing algorithms tend to focus on interpreting changes in the diffraction pattern using the gnomonic projection, i.e., how the pattern is presented with respect to a flat 2D capturing screen [3]. In this manuscript, we present new algorithms that exploit the fact that the EBSP is generated from a point source and is therefore more properly rendered onto the surface of a sphere [4]. For band localisation and conventional indexing, this is advantageous as the spherical Radon transform accounts for the band shape properly, because bands are parallel edged when rendered as great circles on the sphere. For the cross correlation method, a spherical matching process reduces template matching to a one-to-one correlation with alignment in $SO(3)$ directly and avoids the need of generating an expansive number of templates in gnomonic projections from a master pattern [5].

The electron backscatter diffraction pattern (EBSP) is generated as electrons enter the sample, scatter and dynamically diffract. For an introduction to conventional EBSD analysis, see the review article by Wilkinson and Britton [1]. In practice, diffracting electrons are captured using a flat screen inserted within the electron microscope chamber. The result of this dynamical diffraction process is the generation of an EBSP that contains bands of raised intensity which are called the “Kikuchi bands”. The centre line of each band **corresponds to** a plane that contains the electron source point and is parallel to the diffracting crystal plane. The edges of the bands are two Kossel conic sections separated by 2θ . The dynamical diffraction process is explained in greater detail in the work of Winkelmann et al. [6] and now

provides us high quality simulations that contain significant crystallographic information, such as the intensity profile near a zone axes. These simulated patterns more accurately reproduce the intensity distributions found within experimentally captured patterns, ~~as compared to simple kinematic models~~. This development has spurred an interest in using these patterns for direct orientation determination. ~~comparison with experiments to improve robustness and precision, rather than the conventional image based analysis using the Hough or Radon transforms.~~

The Hough transform has been used to render the bands within the EBSP as points within a transformed space for easy localisation using a computer [7]. In these conventional algorithms, we assume that the bands within the EBSP are near parallel for their localisation within Radon space and we tend to locate the band centres. This renders localisation of the bands into the computationally simpler challenge of finding peaks of high intensity within a sparsely populated space. Unfortunately, within the gnomonic projection the edges of the bands are not parallel. Additionally, the Hough transform of the bands produces butterfly artefacts which makes precise and robust localisation of the bands challenging. However, if the bands are presented as rings on the surface of the sphere [4] there is potential to integrate intensity profiles more precisely. This is advantageous for geometries where there may be divergence of the bands (e.g. low voltage or where the pattern centre is less central).

To advance our analysis further, peak localisation and indexing may not be needed if we can efficiently directly compare and match the intensity distributions found within ~~a~~ high quality simulation against our experimental pattern. This can be performed with cross correlation (i.e. finding a peak in the associated cross correlation function), which underpins template matching based EBSD analysis, including the “dictionary indexing” method [5] and template matching approaches [8, 9]. At present, template matching has been performed in the gnomonic frame where a “master pattern” is re-projected into (gnomonic) detector frame. As we know the pattern can be represented on the surface of a sphere, we can change this approach to use one master sphere and best align the orientation O of our test crystal by rotating the experimentally re-projected sphere to best overlap the master sphere (with care with regards to symmetry).

Existing cross correlation methods [10, 5, 8, 9] are performed within the gnomonic projection of the detector. Hereby, each measured Kikuchi pattern P_{ij} is compared with a reference

pattern $S_{ij}(\mathbf{O})$ according to a test orientation \mathbf{O} . The fit between both images is commonly measured by their correlation

$$C(P, S(\mathbf{O})) = \sum_{ij} P_{ij} S_{ij}(\mathbf{O}) \quad (1.1)$$

where the sum is over all pixels in the pattern.

For template matching, reference patterns are tested according to multiple orientations until the best match is found. Sampling of the orientations is performed with a desired angular resolution (sufficient to find a peak and related to the ultimate angular sensitivity). This is computationally very expensive as the above sum has to be computed for a sufficiently large number of reference patterns $S_{ij}(\mathbf{O}_m)$, $m = 1, \dots, M$ to have a good estimate of the true orientation of the measured Kikuchi pattern P_{ij} . Recently, Foden et al. [8] have presented an alternative approach where use of a FFT-based cross correlation, with a wider and higher contrast correlation peak, is combined with a subsequent orientation refinement step to interpolate between library patterns to provide a more computationally efficient method of template matching. However, that method still involves an expensive gnomonic based library search.

In this work we address this efficiency problem and perform the matching directly on the surface of the sphere. Therefore, we require only one spherical master pattern. In this paradigm different orientations results in different rotations of the spherical master pattern. The central idea of this paper is to represent the correlation function between the experimental Kikuchi pattern and all rotated versions of the spherical master pattern as a spherical convolution which can be computed using fast Fourier techniques.

In the case of plane images P_{ij} and S_{ij} it is well known [11] that the correlation image

$$C_{k,\ell} = \sum_{i,j} P_{ij} S_{i+k,j+\ell}$$

with respect to all shifts k, ℓ can be computed simultaneously using the fast Fourier transform \mathcal{F} . More precisely, we have

$$C = \mathcal{F}^{-1}(\mathcal{F}P \odot \mathcal{F}S)$$

where \odot denotes the pointwise product. Such Fourier based algorithms have approximately square root the number of operations compared with direct algorithms.

The match between two spherical diffraction patterns can be measured through spherical cross correlation resulting in a function on orientation space. The position of the maximum peak of this function directly gives the desired misorientation of the experimental pattern with respect to the master pattern. In order to speed up the computation of the spherical cross correlation function we apply the same Fourier trick as explained above. In short, we compute spherical Fourier coefficients of the experimental and the master pattern, multiply them and obtain a series representation of the cross correlation function with respect to generalised spherical harmonics. Computation of the spherical Fourier coefficients and evaluation of the generalised spherical harmonics is done using the nonequispaced fast Fourier transform (NFFT) which is at the heart of the MTEX toolbox used for texture analysis. The NFFT builds upon significant research generalising the FFT to non Euclidean domains, e.g. to the sphere, cf. [13, 14], or the orientation space, cf. [15] and to apply them to problems in quantitative texture analysis, cf. [16, 17, 18, 19]. Although our algorithm are theoretically fast the running times of our implementations are behind those of well established methods. The main reason for this is that our implementations are not yet optimised to take advantage of crystal symmetries, computing on the graphics card or any other kind of parallelisation. On the other hand, this keeps our proof of concept code very simple and allows for easy customisation.

2. Spherical Diffraction Patterns

The advantages of considering Kikuchi patterns as spherical functions have been explained very nicely by Day [4]. For the present method, each point on the surface of the sphere can be modelled as a diffraction vector from the crystal which is located at the centre of the sphere. If we rotate the crystal, the sphere rotates, and therefore our challenge is to either index each band within the sphere or to locate a rotation matrix which rotates one experimental sphere onto the sphere with a reference orientation.

We start the development of our algorithms with a high quality dynamical simulation of alpha-Iron (BCC) generated within DynamicS and project it using image interpolation onto the surface of the sphere. The commercial program uses dynamical theory presented by Wikelmann et al. [6] to calculate the intensity of electrons in the resultant diffraction pattern (with no background contributions).

For an experimental pattern the diffraction sphere is not completely described as the

detector does not subtend all diffraction angles. The amount of the sphere subtended is described by the shape, size and detector distance. The gnomonic projection can be used to interpolate a subregion of the sphere and we can use a gnomonic reprojection to go from the screen to the sphere. For our algorithms the **incomplete coverage** causes two issues: (1) edge effects due to a break in periodicity, which can be resolved by appropriate use of windowing functions; (2) incomplete Kikuchi bands which leads to different peak intensities in the spherical Radon transform. We will address these in more detail within Sec. 4.

3. Harmonic Approximation on the Sphere

Simulated as well as experimental Kikuchi pattern can be interpreted as diffraction intensities f_j with respect to discrete diffraction directions ξ_j that can be computed from the position within the pattern by the inverse gnomonic projection. For our algorithms, we are interested in approximating these intensities f_j by a smooth spherical function $f: \mathbb{S}^2 \rightarrow \mathbb{R}$, represented by a series expansion of the form

$$f(\xi) = \sum_{n=0}^N \sum_{k=-n}^n \hat{f}(n, k) Y_n^k(\xi), \quad (3.1)$$

such that $f(\xi_j) \approx f_j$. Hereby, Y_n^k denotes the spherical harmonics which replace the exponential functions in the classical Fourier transform. Similarly to the classical case many properties of the function f can be directly derived from its Fourier coefficients $\hat{f}(n, k)$. If we consider f as an image on the sphere, many image operations, like convolution, rotation or differentiation, can be efficiently described in terms of the Fourier coefficients (see Figure 3.1a).

There exist several methods for determining the coefficients $\hat{f}(n, k)$ in (3.1) from discrete diffraction intensities $f(\xi_j)$. Three of those will be introduced shortly: quadrature, interpolation, and approximation.

3.1. Quadrature

The quadrature based approach exploits the fact that the spherical harmonics Y_n^k form an orthonormal basis with respect to the inner product

$$\langle f_1, f_2 \rangle = \int_{\mathbb{S}^2} f_1(\xi) \overline{f_2(\xi)} d\xi.$$

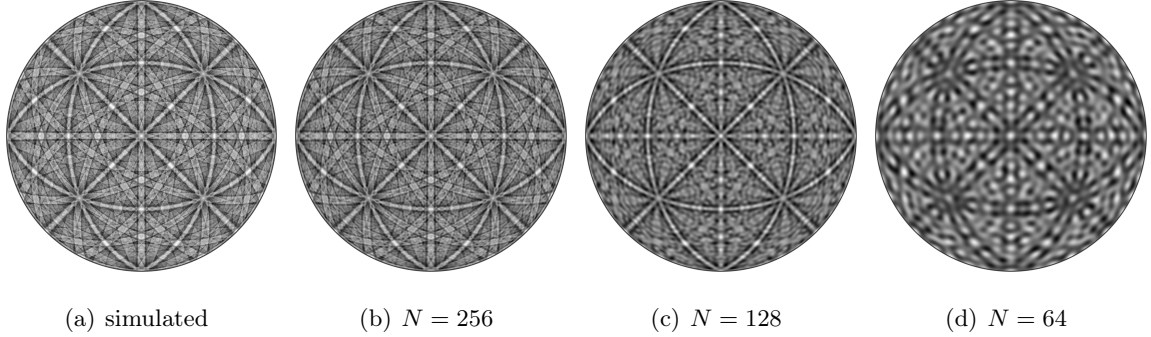


Figure 3.1 – Stereographic projection of the dynamically simulated Kikuchi pattern for iron (a) and its approximation by spherical harmonics with different harmonic degrees N .

As a consequence, the expansion coefficients $\hat{f}(n, k)$ satisfy

$$\hat{f}(n, k) = \int_{\mathbb{S}^2} f(\boldsymbol{\xi}) \overline{Y_n^k(\boldsymbol{\xi})} d\boldsymbol{\xi}.$$

Computing this integral numerically is called quadrature and leads to sums of the form

$$\hat{f}(n, k) \approx \sum_{j=1}^J \omega_j f(\boldsymbol{\xi}_j) \overline{Y_n^k(\boldsymbol{\xi}_j)}, \quad (3.2)$$

with the quadrature nodes $\boldsymbol{\xi}_j \in \mathbb{S}^2$ and quadrature weights $\omega_j \in \mathbb{R}$, $j = 1, \dots, J$. The challenge is to find those nodes and weights such that the approximation is as good as possible. Good choices are discussed in [20, 21] and the references therein.

Evaluating the sum (3.2) for $n = 0, \dots, N$ and $k = -n, \dots, n$ directly would require $N^2 \cdot J$ numerical operations. Fortunately, this sum can be computed much faster using the nonequispaced fast Fourier transform [22] requiring only $N^2 \log N + J$ numerical operations.

The key parameter when approximating a spherical function by its harmonic series expansion is the cut-off frequency N . Figure 3.1 illustrates the effect of this cut-off frequency N when approximating a Kikuchi pattern. We observe that a cut-off frequency of $N = 128$ gives sufficient details of a typical pattern.

The advantage of the quadrature based approach is its simplicity. This comes at the cost that the function values of f have to be known at the specific quadrature nodes $\boldsymbol{\xi}_j$, which can be true for simulated patterns but will not be true for experimental patterns.

3.2. Interpolation and approximation

If the function f to be approximated is given at discrete points $\boldsymbol{\xi}_j$, $j = 1, \dots, J$, i.e., $f(\boldsymbol{\xi}_j) = f_j$, for which no quadrature rule is known we may compute the expansion coefficients

$\hat{f}(n, k)$ by solving the system of linear equations

$$\sum_{n=0}^N \sum_{k=-n}^n \hat{f}(n, k) Y_n^k(\xi_j) = f_j. \quad (3.3)$$

It should be noted that this system of linear equations may become ill conditioned, especially in the case that the number of interpolation nodes J equals the number $(N + 1)^2$ of coefficients $\hat{f}(n, k)$. It is therefore recommended to consider the underdetermined or overdetermined problem and solve it using the normal equation of first or second kind, respectively.

Interpolation corresponds to the underdetermined case where the system of equations (3.3) has no unique solution. To restore uniqueness we search for coefficients solving (3.3) and simultaneously minimising some functional $\varphi(\hat{f})$ which characterises the smoothness of f . Common choices are Sobolev norms of order $s > 0$,

$$\varphi(\hat{f}) = \sum_{n=0}^N \sum_{k=-n}^n (n + 1)^s |\hat{f}(n, k)|^2.$$

The solution of this constrained minimisation problem can be found by solving the corresponding normal equation of second kind. See also [23] for more details on the stability of spherical interpolation.

In the case of experimentally measured data it can be easier and more stable to solve an approximation problem instead of an interpolation problem, i.e. we are in the overdetermined case and the system of equations (3.3) must not have any solution. We therefore look for the coefficients $\hat{f}(n, k)$ which achieve the smallest error

$$F(\hat{f}) = \sum_{j=1}^J \left(\sum_{n=0}^N \sum_{k=-n}^n \hat{f}(n, k) Y_n^k(\xi_j) - f_j \right)^2 + \lambda \sum_{n=0}^N \sum_{k=-n}^n (n + 1) |\hat{f}(n, k)|^2$$

while decaying to zero quickly. Here the first summand measures the fitting of the approximation in the points ξ_j and the second summand is the regularisation term that measures the smoothness of the function and punishes noise. The weighting between these two terms is accomplished via the parameter λ which is often called regularisation parameter and has to be chosen such that there is balance between these two contradicting terms.

As an example, Figure 3.2 depicts an “experimental” Kikuchi pattern 3.2(a) together with a quadrature based 3.2(b) and approximation based 3.2(c) representation with respect to spherical harmonics. We observe that the approximation based approach leads to severe

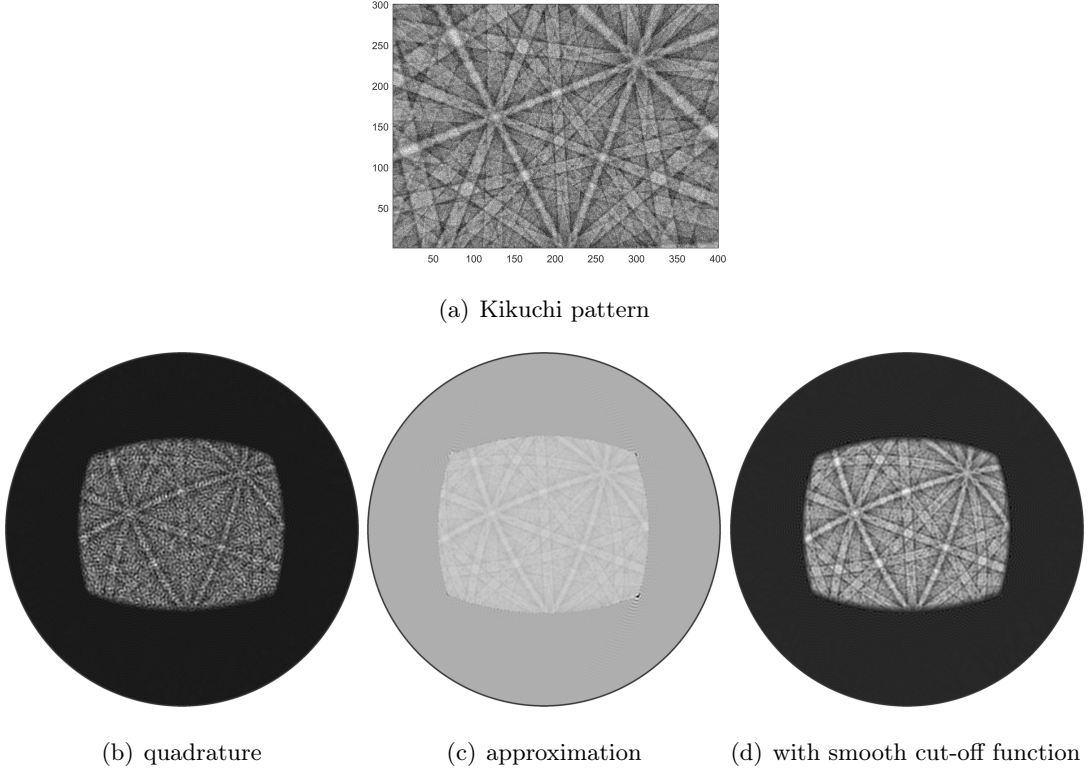


Figure 3.2 – Spherical approximations of a simulated Kikuchi pattern at a detector corrupted by noise.

artefacts close to the detector boundaries. The reason is that harmonic functions are very bad in representing functions with hard jumps. This problem can be significantly relaxed by multiplying the data with filter that generates a smooth decay from the values inside the detector to zero outside the detector. The resulting harmonic approximation is displayed in 3.2(d).

4. Spherical Radon transform based band detection and indexing

In conventional EBSD indexing the Kikuchi pattern represented in the gnomonic frame is summed up along all straight lines resulting in [the](#) Radon transform. Since in the Radon transform diffraction bands appear as local extrema they can be found by a peak detection algorithm. A severe problem of this approach is that due to the gnomonic projection bands in the Kikuchi pattern do not appear as straight features but have hyperbolic shape. As a consequence the local extrema are less sharp which negatively affects the accuracy and robustness of this approach. An alternative band analysis method which correctly uses the

fact that the parallel bands on the surface of a sphere are well represented as hyperbolic sections in the gnomonic frame is incorporated in the 3D Hough transform [24].

In this section we will make use of the fact that Kikuchi bands on the sphere are great circles and can be efficiently detected by a spherical Radon transform and its generalisations. Once sufficiently many bands are located the orientation can be determined by conventional indexing algorithms, e.g. with AstroEBSD [25].

4.1. The spherical Radon transform

The spherical Radon transform integrates a function on the sphere along all great circles, which is similar to how the ordinary Radon transform (or Hough transform) integrates an image along all lines. Such a great circle \mathcal{C} on the sphere can be described as the set of all points $\xi \in \mathbb{S}^2$ that are orthogonal to a given normal vector $\eta \in \mathbb{S}^2$, i.e., $\mathcal{C}(\eta) = \{\xi \in \mathbb{S}^2 \mid \xi \cdot \eta = 0\}$. Accordingly the spherical Radon transform

$$g(\eta) = \mathcal{R}f(\eta) = \int_{\mathcal{C}(\eta)} f(\xi) d(\xi). \quad (4.1)$$

of a spherical function $f: \mathbb{S}^2 \rightarrow \mathbb{R}$ is again a spherical function $g: \mathbb{S}^2 \rightarrow \mathbb{R}$.

The crucial point is now, that the Fourier representation of g can be computed straight forward from the Fourier coefficients $\hat{f}(n, k)$ of f , i.e., we have

$$g(\eta) = \sum_{n=0}^N \sum_{k=-n}^n P_n(0) \hat{f}(n, k) Y_n^k(\eta), \quad (4.2)$$

where P_n are the Legendre polynomials. The practical use of this formula is that for computing the Funk transform of a spherical image we do not need to average the pixel values along all great circles but, instead, compute the Fourier coefficients of the spherical image, multiply them with

$$P_n(0) = \begin{cases} (-1)^{n/2} \frac{(n-1)(n-3)\cdots 3 \cdot 1}{n(n-2)\cdots 4 \cdot 2}, & n \text{ is even} \\ 0, & n \text{ is odd} \end{cases}$$

and apply the spherical Fourier transform which gives us the spherical image of the Funk transform. For an image of $m \times m$ pixels the later algorithms using the nonequispaced fast spherical Fourier transform [14] is about m times faster. In Figure 4.1 the spherical Radon transform of the Kikuchi pattern from Figure 3.1 is depicted for different choices of the cutoff frequency N .

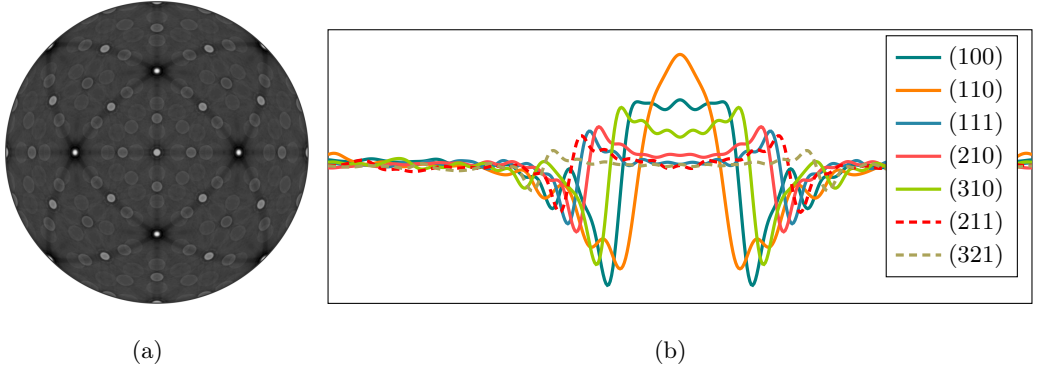


Figure 4.1 – (a) Spherical Radon transform of the master pattern. (b) Integrals around the plane normals within the Radon transform to reveal the band profiles.

Fig. 4.1a shows the spherical Radon transform of the dynamically simulated master pattern from Fig. 3.1. The circular features correspond to the bands in the Kikuchi pattern. As the master pattern is known on the entire sphere its Radon transform covers the whole sphere as well.

4.2. Spherical convolution and band localisation

The brightness and sharpness of the Radon peaks corresponding to each lattice plane is not uniform in Fig. 4.1a which is determined by dynamical diffraction associated with each crystalline lattice plane. We can assess this structure by integrating the spherical diffraction pattern about all rotations $R_{\boldsymbol{\eta}}(\omega)$ about the plane normal $\boldsymbol{\eta}$

$$\Phi_{\text{sim}}(\boldsymbol{\xi}) = \int_0^{2\pi} f_{\text{sim}}(R_{\boldsymbol{\eta}}(\omega)\boldsymbol{\xi}) d\omega$$

within the simulated master pattern f_{sim} . In case the plane normal $\boldsymbol{\eta}$ coincides with the z -axis the profile Φ_{sim} is given by the Legendre series

$$\Phi_{\text{sim}}(\boldsymbol{\xi}) = \sum_{n=0}^N \hat{f}_{\text{sim}}(n, 0) P_n(\boldsymbol{\xi} \cdot \boldsymbol{\eta})$$

with $\hat{f}_{\text{sim}}(n, 0)$ being a subset of the Fourier coefficients of f_{sim} . In the general case of an arbitrary plane normal, it is sufficient to rotate f_{sim} such that the plane normal aligns with the z -axis and to proceed as above. The resulting band profiles for the major bands in cubic materials are depicted in Fig. 4.1.

We use our knowledge of these band profiles to identify peaks within spherical Radon transform of the experimental patterns using spherical convolution

$$f \star \Phi(\boldsymbol{\eta}) = \int_{\mathbb{S}^2} f(\boldsymbol{\xi}) \Phi(\boldsymbol{\xi} \cdot \boldsymbol{\eta}) d\boldsymbol{\xi}. \quad (4.3)$$

of the pattern f with a specific band profile Φ . The spherical convolution with a band profile can be seen as a generalisation of the spherical Radon transform. Indeed, choosing as the band profile $\Phi = \delta$ the delta distribution the spherical convolution $f \star \Phi = \mathcal{R}f$ coincides with the spherical Radon transform. Luckily, the convolution $f \star \Phi$ can be computed as fast as the spherical Radon transform in Fourier space by the formula

$$f \star \Phi(\boldsymbol{\eta}) = \sum_{n=0}^N \sum_{k=-n}^n \hat{\Phi}(n) \hat{f}(n, k) Y_n^k(\boldsymbol{\eta}) \quad (4.4)$$

where $\hat{\Phi}(n)$ denotes the Legendre coefficients of the band profile Ψ .

In Fig. 4.2(a) and 4.2(b) the spherical convolution of the master pattern with band profiles corresponding to planes (211) and (310) has been plotted. We observe extremely sharp peaks at the corresponding band positions. The other bands are not as pronounced, as they less well match the convolution template. Hence, we use an approximate band profile Ψ which allows for the reliable detection of all the major bands. Fig. 4.2(c) and 4.2(d) give reasonable choices of such band profiles. In our subsequent analysis we rely on the modified Gaussian band profile

$$\Psi(\cos \omega) = \exp\left(-\frac{(\omega - 90)^2}{9}\right) - \exp\left(-\frac{(\omega - 93)^2}{4}\right) - \exp\left(-\frac{(\omega - 87)^2}{4}\right) \quad (4.5)$$

in 4.2(d) (with an average band width tailored for our accelerating voltage). The spherical convolution of the Kikuchi pattern is a generalisation of the butterfly mask [7] and the top hat filter [26] used in conventional Radon/Hough based EBSD.

4.3. Peak detection

In the conventional Radon/Hough transform approach for band detection in Kikuchi pattern, the numbers of pixels in the Radon transform is approximately the same as in the input (resized) Kikuchi pattern. This limits the possible resolution of the orientations determined¹.

¹The resolution of Radon/Hough based approaches is a combination of the resolution of the Radon space, the quality of the diffraction patterns, and the number of bands successfully localised and indexed.

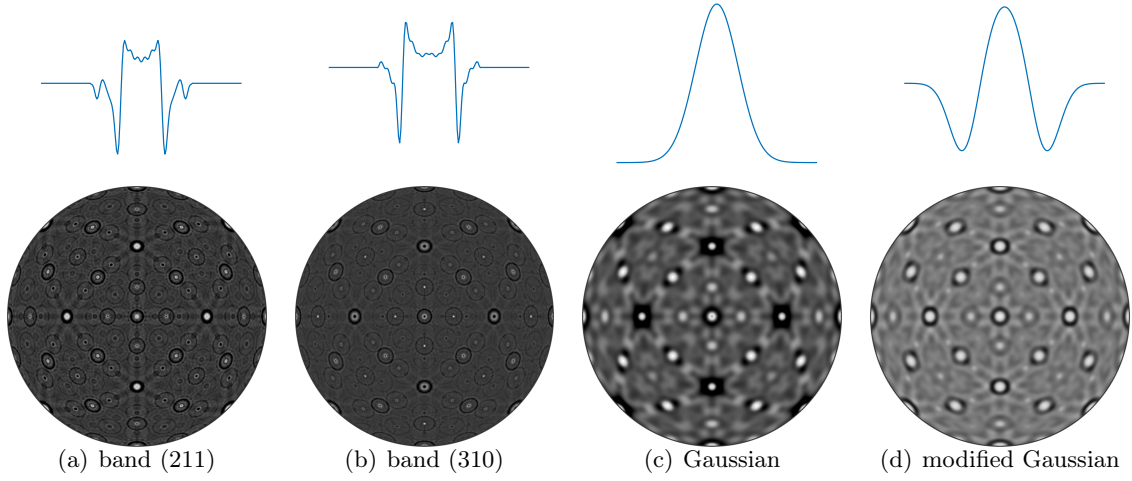


Figure 4.2 – Spherical convolution of the master pattern with different band profiles.

In contrast, when computing the spherical Radon transform according to (4.2) or the spherical convolution by (4.4) such a restriction to a grid of pixels does not exist. Instead, we can evaluate those sums for any normal vector $\boldsymbol{\eta}$. Since it would be way too time consuming to evaluate (4.2) or (4.4) at an arbitrarily fine grid, we propose a simultaneous steepest descent approach to find all local maxima (similar gradient upsampling approaches are commonly used in cross correlation algorithms to refine precision).

The algorithm to find all peaks of a spherical function g is as follows: we start with a set of approximately equispaced points $\boldsymbol{\eta}_m$, $m = 1, \dots, M$ on the sphere. Then we compute all the gradients $\nabla g(\boldsymbol{\eta}_m)$, $m = 1, \dots, M$ of g according to the formulae

$$\begin{aligned} \partial_\rho g(\boldsymbol{\eta}(\theta, \rho)) &= \sum_{n=0}^N \sum_{k=-n}^n ik\hat{g}(n, k)Y_n^k(\boldsymbol{\eta}), \\ \partial_\theta g(\boldsymbol{\eta}(\theta, \rho)) &= \sum_{n=0}^N \sum_{k=-n}^n k\hat{g}(n, k)Y_n^k(\boldsymbol{\eta}), \\ \nabla g(\boldsymbol{\eta}) &= \frac{1}{\sin \theta} \partial_\rho g(\boldsymbol{\eta}) \mathbf{e}_\rho(\boldsymbol{\eta}) + \frac{1}{\sin^2 \theta} \partial_\theta g(\boldsymbol{\eta}) \mathbf{e}_\theta(\boldsymbol{\eta}) \end{aligned} \quad (4.6)$$

using the fast spherical Fourier transform and maximize g locally along the lines

$$\boldsymbol{\eta}_m^1 = \boldsymbol{\eta}_m + \lambda_m^1 \nabla g(\boldsymbol{\eta}_m).$$

This procedure is iterated and nodes $\boldsymbol{\eta}_m^\ell$ are found which converge for $k \rightarrow \infty$ to the local maxima of the function g . During the convergence, several of the nodes $\boldsymbol{\eta}_m^\ell$ will converge to the same maxima and, hence, can be merged to one node.

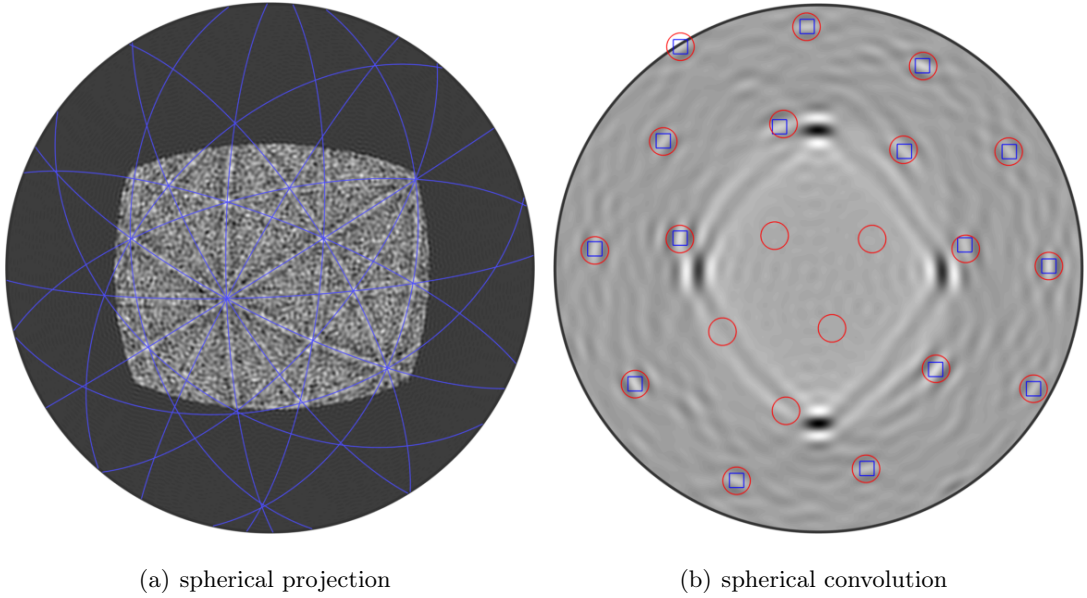


Figure 4.3 – (a) Spherical projection, with bands identified using the spherical Radon transform overlapped (b) Spherical Radon transform with convolution with the band profile from Fig. 4.2(d). Identified bands as blue squares corresponding to white peaks together with the input plane locations as red circles.

An “experimental” pattern (a simulation with added noise) is transformed to the sphere and the spherical Radon transform is applied. Contrast normalisation is applied, to manage the incomplete population of diffraction vectors for the surface of the spherical pattern.

Peaks are localised within this Radon transform using convolution with the modified Gaussian profile (Fig. 4.2d).

4.4. Optimising spherical Radon based indexing accuracy

Once a certain number of bands have been detected in the Kikuchi pattern any of the well known indexing algorithms, e.g. [27, 25], can be used for determining the corresponding orientation. We utilise AstroEBSD [25] and optimise parameters within the spherical Radon transform to improve the measurement of crystal orientation as determined by the precision of the localisation of peaks.

To refresh, our spherical Radon based indexing algorithm involves:

1. Project the experimental diffraction pattern onto the surface of a sphere
2. Approximate the discrete pattern by a spherical Fourier series as per equation (3.1).

3. Compute the spherical convolution (4.4) with a suitable band profile in Fourier space.
4. Detect the most pronounced peaks in the spherical convolution and search for their centres.
5. Use an indexing method (e.g. AstroEBSD) to determine the crystal orientation.
6. If needed, this crystal orientation can be transformed into another frame (e.g. from the detector frame to the sample frame).

In step 1, the pattern centre must be known. In step 2, we choose the harmonic cut-off frequency N . In step 3, we choose a suitable band profile (which matches the bands expected in our lookup table). In step 4, the number of iterations and the resolution of the initial search grid is crucial. In step 5, we select the number of bands used for indexing.

The number of bands used to index will depend on the population of the look-up table in the indexing method and the indexing algorithm used. Too few bands will result in mis-indexing (e.g. due to pseudosymmetry). Too many bands will slow down indexing and can cause inaccuracies due to mis-indexing of plane families. For the indexing BCC-iron aiming to solve for between 8-12 bands is usually reasonable, and therefore we have selected to search for 10 bands here.

To identify bands, we have selected an idealised band profile, calibrated using our master pattern which is the modified Gaussian (presented in 4.2d). For less symmetric crystals, this could be tuned through calculation of the convolution of the idealised band profile with the integrals presented in Fig. 4.1b. The performance of our chosen modified Gaussian is shown in 4.2.

Putting everything together and choosing for indexing algorithm AstroEBSD [25] we first verify our method with simulated noisy patterns. We proceed as follows. First we select a random orientation \mathbf{O} . Then we dynamically simulate a corresponding Kikuchi pattern with 400×300 pixel and add noise as displayed in Fig. 4.3(b). We use this pattern to determine an orientation $\tilde{\mathbf{O}}$. Finally, we compute the disorientation between initial orientation \mathbf{O} and the computed orientation $\tilde{\mathbf{O}}$. Histograms of these disorientation angles for different harmonic cut-off degrees N are depicted in Fig. 4.4. We determine that a mean accuracy of 0.1° can be obtained.

In Sec. 6 we will utilise this indexing algorithm to determine orientations for an experimental data set.

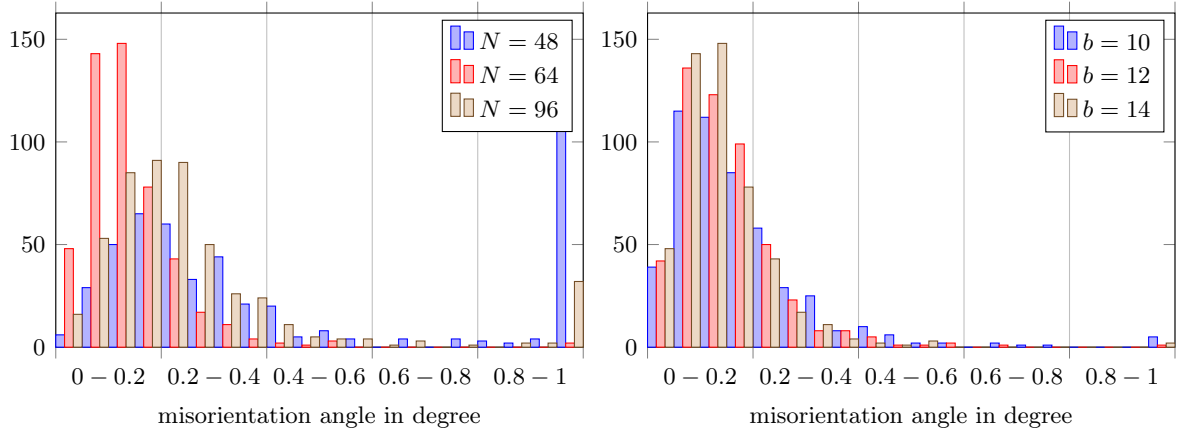


Figure 4.4 – Histograms of the disorientation between the original orientation and the orientation determined by spherical band detection. Left histogram fixes the number of bands $b = 14$ and varies the harmonic cut-off degrees N and right histogram fixes the harmonic cut-off degrees $N = 64$ and varies the number of bands b .

5. Spherical cross correlation based indexing

We have established that experimental and master pattern can be well represented by their harmonic expansion on the sphere and that this representation is useful for band detection. Now we present the use of this representation when computing the cross correlation between an experimental pattern with all possible rotations of a master pattern.

Template matching of EBSD patterns usually employs the following steps:

1. Simulate a dynamical master pattern of all orientation vectors.
2. Select a dense set of orientations \mathbf{O}_m , $m = 1, \dots, M$.
3. Project the master pattern for each orientation a Kikuchi pattern S_{ij}^m at the detector to create a library.
4. For each pattern S_{ij}^m within the library compute the cross correlation with each experimental pattern P_{ij} .
5. Select the orientation \mathbf{O}_m with the largest cross correlation value $C(m)$ as the indexed orientation.

The main advantage of this template matching based cross correlation approach is that it performs direct matching of all diffraction pattern features through intensity based cross correlation, and does not reduce indexing to a simple “geometry” based problem of localising and indexing the bands. This provides the potential that this method is more robust to noise.

The main disadvantage of the template matching based cross correlation approach is that reprojection of the master pattern for a dense population of orientation space is memory intensive and repeated cross correlation of each experimental pattern with the library is computationally expensive.

Therefore, in this section we transfer the cross correlation based approach to our spherical setting, i.e., we compute the cross correlation (1.1) with respect to smooth functions on the sphere and not pixel by pixel on the detector.

5.1. Spherical cross correlation

We start by representing both the simulated pattern as well as the experimental pattern by expansions in spherical harmonics

$$f_{\text{sim}}(\mathbf{h}) = \sum_{n=0}^N \sum_{k=-n}^n \hat{f}_{\text{sim}}(n, k) Y_n^k(\mathbf{h}) \quad (5.1)$$

$$f_{\text{exp}}(\mathbf{r}) = \sum_{n=0}^N \sum_{k'=-n}^n \hat{f}_{\text{exp}}(n, k') Y_n^{k'}(\mathbf{r}) \quad (5.2)$$

as discussed in Sec. 3. Note, that the simulated pattern f_{sim} is usually represented with respect to crystal coordinates, while the experimental pattern f_{exp} is represented with respect to detector coordinates. Let \mathbf{O} be the exact crystal orientation of the experimental pattern, i.e., $\mathbf{r} = \mathbf{O}\mathbf{h}$. Then the basic assumption of the pattern matching approach is that the simulated pattern transformed into the specimen reference frame gives a good approximation of the experimental pattern modulo a scaling factor α , i.e.

$$f_{\text{exp}}(\mathbf{r}) \sim \alpha f_{\text{sim}}(\mathbf{O}^{-1}\mathbf{h}).$$

The similarity of two spherical functions modulo a rotation \mathbf{O} can be measured by the spherical cross correlation, which is defined as the integral of the product of both functions over the entire sphere

$$C(f_{\text{sim}}, f_{\text{exp}})(\mathbf{O}) = \int_{\mathbb{S}^2} f_{\text{sim}}(\mathbf{O}^{-1}\mathbf{r}) f_{\text{exp}}(\mathbf{r}) \, d\mathbf{r} = \int_{\mathbb{S}^2} f_{\text{sim}}(\mathbf{h}) f_{\text{exp}}(\mathbf{O}\mathbf{h}) \, d\mathbf{h}. \quad (5.3)$$

In order to evaluate these integrals numerically one could make use of a spherical quadrature rule with nodes \mathbf{h}_n and weights ω_m , cf. Sec. 3.1, which leads to the sum

$$C(f_{\text{sim}}, f_{\text{exp}})(\mathbf{O}) = \sum_{n=1}^N \omega_n f_{\text{sim}}(\mathbf{h}_n) f_{\text{exp}}(\mathbf{O}\mathbf{h}_n). \quad (5.4)$$

This sum does not require to pre-compute and store a dictionary of simulated patterns. Instead it is sufficient to store the simulated master pattern f_{sim} at the quadrature nodes \mathbf{h}_n and instead transform each experimental pattern to the sphere. Furthermore, it can be evaluated at arbitrary orientations \mathbf{O} , i.e, we are not restricted to any grid in the orientation space.

5.2. Fast evaluation of the spherical cross correlation

A critical disadvantage of the template matching approach is its high computational costs. Indeed, evaluating the cross correlation function (1.1) at a dense set of M orientations for patterns with N^2 points requires $M \cdot N^2$ numerical operations. Evaluating the spherical cross correlation function (5.4) directly would lead to the same amount of numerical operations. In this section we show how fast Fourier techniques on the orientation space can be exploited to speed up this computation to only $N^3 \log N + M$ numerical operations.

The idea is to use the following important relationship between spherical harmonics Y_n^k and Wigner-D functions $D_n^{k,k'}$, cf. [16],

$$D_n^{k,k'}(\mathbf{O}) = \int_{\mathbb{S}^2} Y_n^k(\mathbf{O}\mathbf{r}) \overline{Y_n^{k'}(\mathbf{r})} \, d\mathbf{r}$$

which allows us to rewrite the series expansion of the rotated simulated pattern as

$$f_{\text{sim}}(\mathbf{O}^{-1}\mathbf{r}) = \sum_{n=0}^N \sum_{k=-n}^n \sum_{k'=-n}^n D_n^{k,k'}(\mathbf{R}) \hat{f}_{\text{sim}}(n, k') Y_n^{k'}(\mathbf{r}). \quad (5.5)$$

Inserting the series expansions (5.2) and (5.5) into the correlation integral (5.3) and making use of the orthogonality of the spherical harmonic Y_n^k we end up with

$$C(f_{\text{sim}}, f_{\text{exp}})(\mathbf{O}) = \sum_{n=0}^N \sum_{k,k'=-n}^n \hat{f}_{\text{sim}}(n, k) \hat{f}_{\text{exp}}(n, k') D_n^{k,k'}(\mathbf{O}) \quad (5.6)$$

$$= \sum_{n=0}^N \sum_{k,k'=-n}^n \hat{C}(n, k, k') D_n^{k,k'}(\mathbf{O}) \quad (5.7)$$

where we have set $\hat{C}(n, k, k') = \hat{f}_{\text{sim}}(n, k) \hat{f}_{\text{exp}}(n, k')$. The latter sum (5.7) is known as the Fourier transform on the rotation group and can be evaluated at M arbitrary orientations \mathbf{O}_m using only $N^3 \log N + M$ numerical operations by the algorithm described in [15].

In order to illustrate our approach we have chosen a random orientation \mathbf{i} and defined the function $f_{\text{exp}}(\mathbf{r}) = f_{\text{sim}}(\mathbf{O}^{-1}\mathbf{r})$ as a rotated version of our master pattern. In a second step we approximated both pattern by expansions into spherical harmonics up to cut-off degree 512.

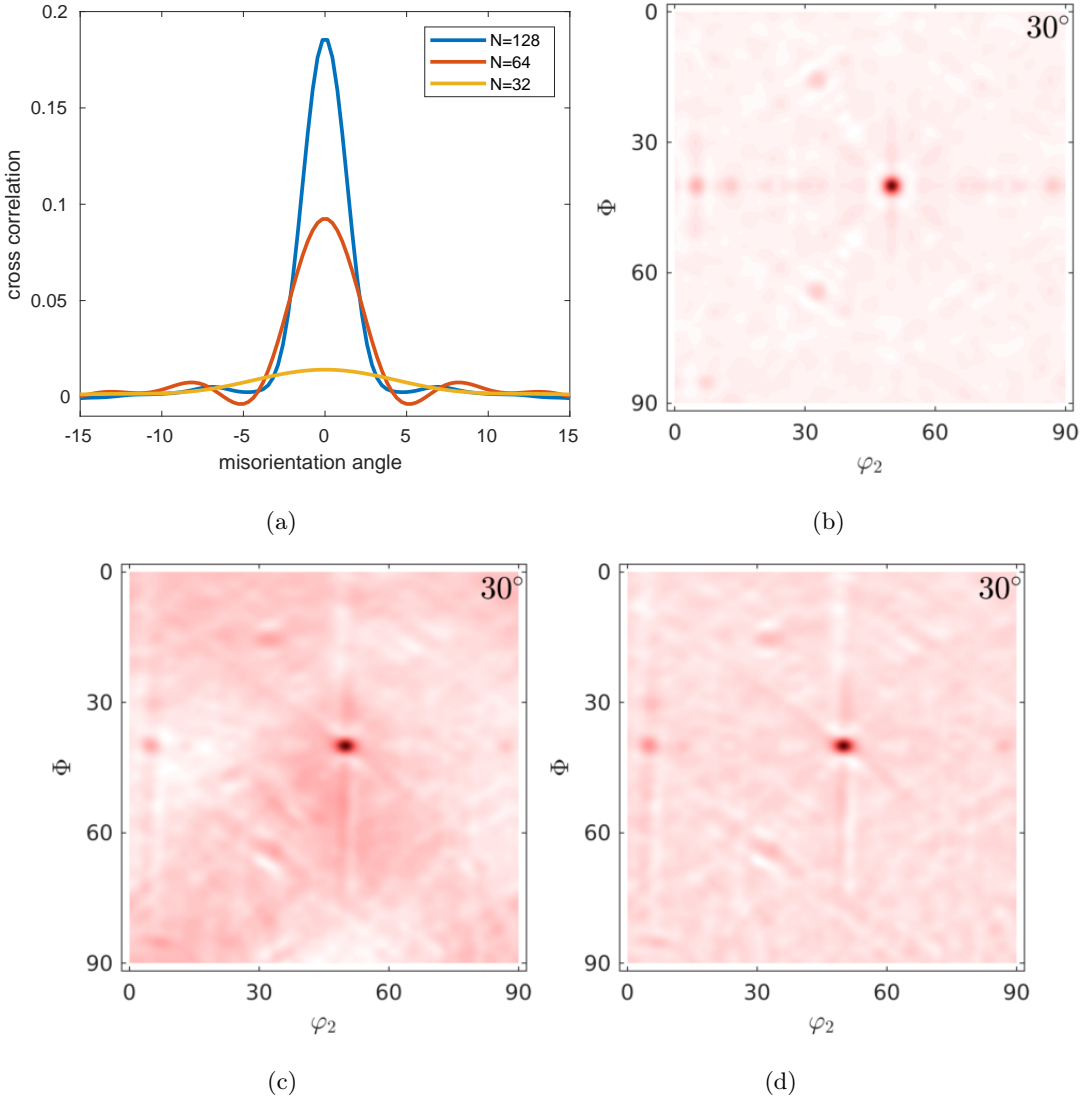


Figure 5.1 – Spherical cross correlation functions: (a) as a function of harmonic cut-off, rotating about the exact orientation; (b) a slice of Euler space showing the presence of a dominant peak (dark red) when compared to the master pattern with a rotated master pattern; (c) the same slide, with an “experimental” pattern correlated against a spherical master, showing the presence of a peak but distortions for incorrect correlations due to the detector windowing artefact; (d) the corrected cross correlation peak accounting for the windowing artefact.

Finally, we calculated the spherical cross correlation function $C(f_{\text{sim}}, f_{\text{exp}})$ as a function of the misorientation from the initial orientation \mathbf{O} for different cut-off degrees N . The results are depicted in Fig. 5.1a. We observe that a cut off degree $N = 64$ gives a good localisation of the peak position close to the true orientation.

5.3. Correction

In the previous section we have assumed that the test pattern f_{exp} is known at the entire sphere. In practice, however, only the projection of the detector back to the sphere is known (as we noted for the band detection approach) and this can cause artefacts in the cross correlation function as depicted in Fig. 5.1c.

Luckily, these artefacts can be computed explicitly as the spherical cross correlation $C(f_{\text{sim}}, \chi)$ between the simulated Kikuchi pattern f_{sim} on the sphere and the cut-off function χ of the detector region projected to the sphere. The final difference

$$C(\mathbf{O}) = C(f_{\text{sim}}, f_{\text{exp}})(\mathbf{O}) - \frac{\int_{\mathbb{S}^2} f_{\text{exp}}}{\int_{\mathbb{S}^2} \chi} C(f_{\text{sim}}, \chi)(\mathbf{O}) \quad (5.8)$$

is depicted in 5.1(d).

5.4. Peak detection

Peak detection for functions of the form (5.7) can be implemented in a similar manner as explained in Sec. 4.3 for spherical functions since the gradient can again be written as a sum with respect to Wigner-D functions. However, in the present case we are only interested in finding the global maximum (and not many local maxima). This makes it efficient to evaluate the corrected cross correlation function (5.8) on a fixed and uniformly spaced grid of orientations \mathbf{O}_m , $m = 1, \dots, M$ with resolution $\delta^{(1)} \approx 2^\circ$ and choose the orientation \mathbf{O}_m^* with maximum function value $C(\mathbf{O}_m)$. In a second step we choose a local grid around the orientation \mathbf{O}_m^* with radius $\delta^{(1)}$ and resolution $\delta^{(2)} \approx 0.1^\circ$ and repeat the calculation. The global resolution needs to be chosen such that no peak falls between the grid points.

5.5. Accuracy determination for spherical cross correlation

We perform a numerical experiment to test the accuracy of our spherical cross correlation algorithm and optimise crucial parameters such as the harmonic cut off degree N as well as the resolutions $\delta^{(1)}$ and $\delta^{(2)}$ of the global and local search grids:

1. Using a dynamical master pattern, generate an approximation using a spherical Fourier series f_{sim} as described in Sec. 3.2.
2. Generate an “experimental pattern” from the master sphere for a random crystal orientation and detector position.

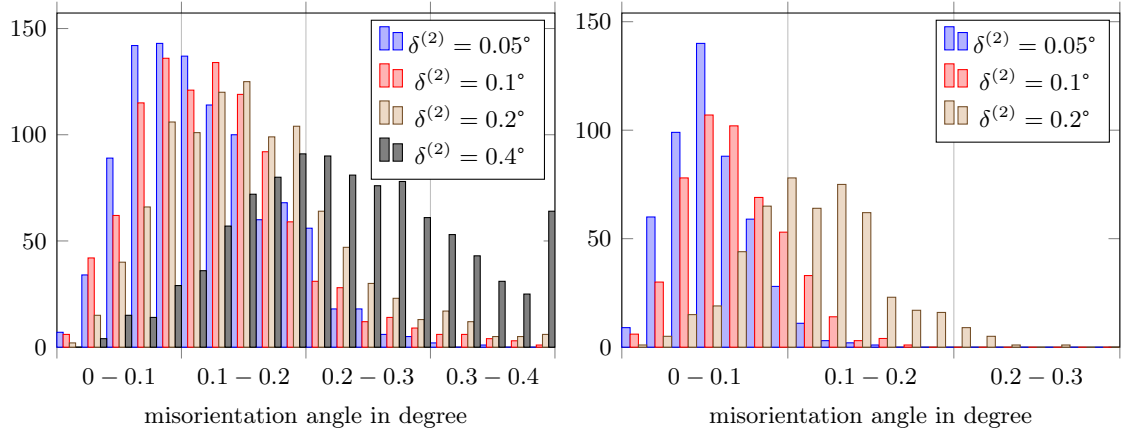


Figure 5.2 – Misorientation angle histograms between the “true” random orientation used for simulating the diffraction pattern and the orientation determined by spherical cross correlation. Left histogram fixes harmonic cut-off bandwidth $N = 48$ and right histogram $N = 64$. Only the resolution $\delta^{(2)}$ of the refined grid is given. The corresponding resolution of the global grid can be found in Table 5.1.

3. Add Poisson distributed noise to the simulated Kikuchi pattern at the detector.
4. Project the noisy “experimental pattern” back to the sphere, multiply it by the mask φ and approximate the product by a spherical Fourier series f_{exp} .
5. Evaluate the corrected spherical cross correlation function $C(\mathbf{O}_m)$ between f_{sim} and f_{exp} at the grid orientations \mathbf{O}_m .
6. Determine the grid orientation \mathbf{O}_m^* with the largest cross correlation value.
7. Compute the misorientation angle between the random orientation \mathbf{O} and the indexed orientation \mathbf{O}_m^* .

This numerical experiment has been run 500 times for different choices of the harmonic cut-off bandwidth N and the different resolutions of the search grid \mathbf{O}_m . Table 5.1 summarises the parameters, the run times and the achieved precision. Full histograms of the misorientation angles are depicted in Figure 5.2.

We observe that a global resolution $\delta^{(1)} = 5^\circ$ is to coarse as it leads to about 5 percent completely mis-indexed patterns. For all other parameter choices we obtain reasonable angular precision up to 0.05° with a speed of one pattern per second on an ordinary laptop without any graphic card support.

cutoff	global search grid			local search grid			speed	precision		
	N	res.	$\delta^{(1)}$	points M_1	radius	res.	$\delta^{(2)}$	points M_2	pattern/s	median
48	5°		5°	4 958	0.4°	9 106		1.8	0.22	4.56
48	2.5°		2.5°	39 565	0.2°	9 128		1.5	0.15	0.07
48	1.5°		1.5°	183 035	0.1°	14 005		1.3	0.12	0.06
48	1.5°		1.5°	183 035	0.05°	112 514		1.1	0.11	0.06
64	2.5°		2.5°	39 565	0.2°	9 128		1.4	0.11	0.04
64	1.5°		1.5°	183 035	0.1°	14 005		1.2	0.06	0.03
64	1.5°		1.5°	183 035	0.05°	112 514		1.0	0.05	0.02

Table 5.1 – Indication of computational costs and associated precision for spherical cross correlation. Times are measured on an ordinary laptop.

6. Experimental Demonstration

We test our two spherical algorithms using the demonstration alpha-Iron data set as used in Britton et al. [25] for conventional indexing using a planar Radon transform and the AstroEBSD indexing algorithm. This data can be found on Zenodo <https://zenodo.org/record/1214829>. This data consists of a 9130 point EBSD pattern map. The AstroEBSD background correction was used with operations: hot pixel correction; resize to 300 pixels wide; low frequency Gaussian background division ($\sigma = 4$), performed independently on each detector half, circular radius cropping to 0.95 of the pattern width. All peak ID based indexing was performed using the Iron phase file, with the top 10 bands used in indexing. The flat Radon transform based indexing was performed with 1 degree theta resolution and up to 13 peaks were sought. The pattern centre was optimised by searching for the minimum weighted mean angular error using a 10×10 grid array. The spherical Radon transform based indexing was performed using the idealised profile given in (4.5). The spherical cross correlation based indexing was performed using the harmonic cut-off frequency $N = 64$ and resolutions $\delta^{(1)} = 1.5^\circ$, $\delta^{(2)} = 0.1^\circ$ for the global, respective, local search grid. Results are presented in Fig. 6.1 IPF colouring and axis-angle colouring with respect to the mean grain orientation (with colour keys included for completeness). Orientations for all three methods are reasonably recovered. The smoothness axis-angle plots for the Radon based methods

are similar, where the spherical method performs slightly better near grain boundaries. The spherical cross correlation method is significantly more robust near grain boundaries.

7. Discussion

In this [manuscript](#), we demonstrate that spherical transformations can be used to index and cross correlate EBSD patterns. Our examples using dynamical simulations provide an initial accuracy for the spherical Radon transform where we achieve better than 0.1° for a reasonable harmonic cutoff and number of bands. This is close to the accuracy achievable for simulated patterns with the 2D Radon transform [of a gnomonic projection](#), and may not be the ultimate accuracy of the spherical Radon approach. Perhaps of more interest for advanced pattern analysis is the potential to extract bands from the pattern using the integration approach. This is similar to integrating along the great circles as originally performed by Day [4]. With this transform, there is potential for the shape and symmetry of bands to [be](#) explored with a view to understanding the asymmetry created either by an improper pattern centre [28], a subtle changes in the lattice [24], and band symmetry [29, 30].

Our examples using spherical cross correlation demonstrate the ultimate resolution is dependant upon the input grid size. However use of a subgrid provides a substantive method to refine the accuracy to be $< 0.1^\circ$. The hierarchical approach shown here is similar to the refinement proposed by Foden et al. [8].

Our examples on the iron data set demonstrate that the technique is robust for polycrystalline experimental maps and the data recovered is comparable to alternative analysis approaches.

We [anticipate](#) that the algorithms as presented can be improved to increase robustness and speed, for example through an inclusion of symmetry in the spherical transforms (which would reduce the number of Fourier coefficients) and there are numerical algorithm improvements which will likely be made as this algorithm is used more (e.g. restriction of the mathematics to the real domain). We hope this manuscript demonstrates the elegance of the spherical approach, and the curious reader can explore the supplied code to see how this is implemented in practice.

An important assumption of the spherical method is that we know the pattern centre *a priori*. The pattern centre is important for our analysis, as an incorrect pattern centre will

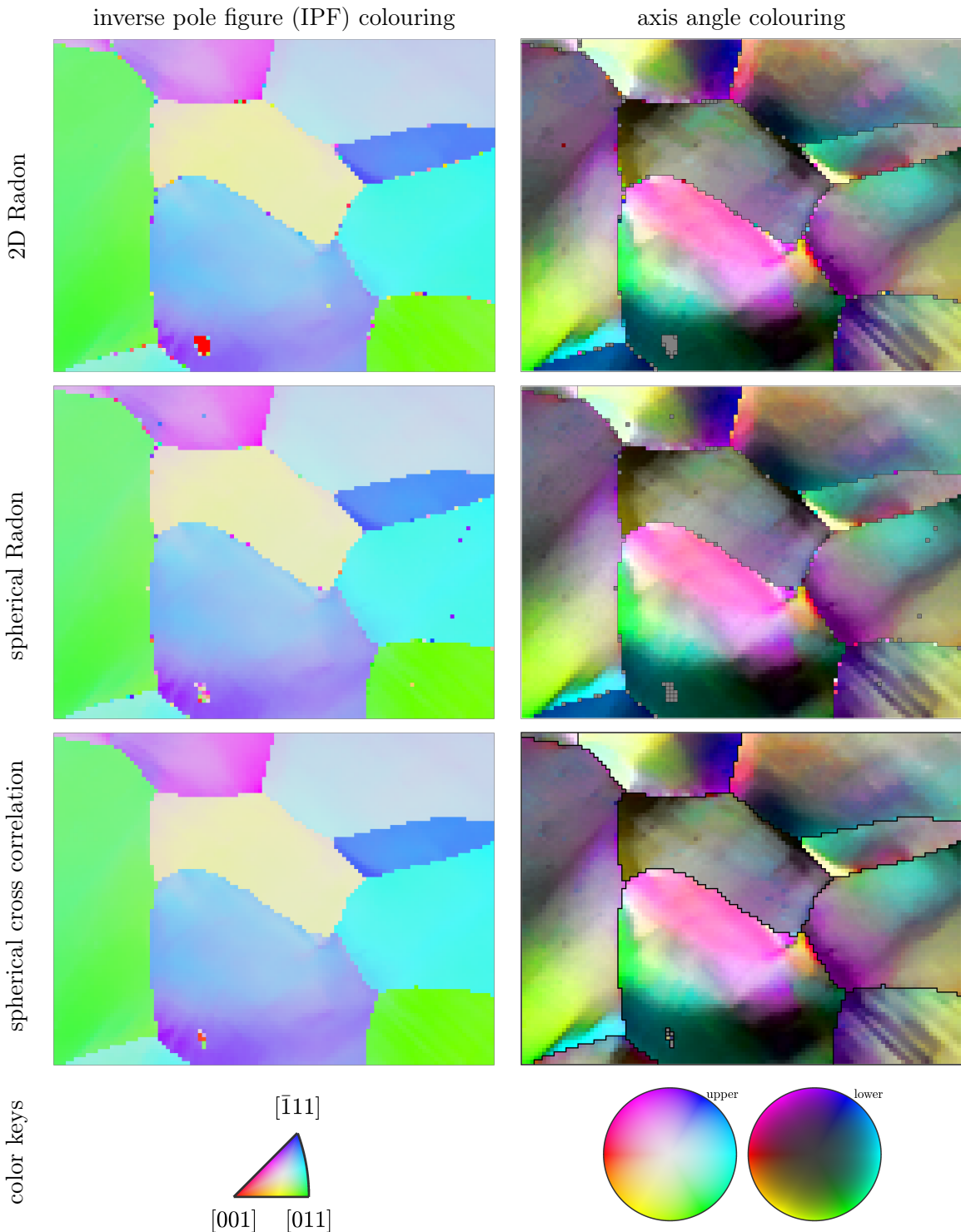


Figure 6.1 – Demonstration alpha-Iron data indexed using 2D based Radon transform band localisation and AstroEBSD indexing, spherical Radon transform band localisation and AstroEBSD indexing, and spherical cross correlation. The IPF colour key is with respect to the horizontal axis. The axis-angle colour key is taken with respect to the mean grain orientation and each key has a radius of 5° .

introduce a distortion on the rendering of patterns on the sphere and the band edges would no longer be parallel. Computationally it can be expensive to optimise the pattern centre based upon this constraint, but there have been suggestions in the literature that centre on this idea (e.g. the 3D Hough [24] and one of the methods of the BYU group [28] in attempting absolute strain measurement with high resolution EBSD). If we assume that we know, or can measure, the pattern centre with reasonable precision with standard methods (e.g. just using the 2D Radon based pattern centre measurements available within commercial or open source software such as AstroEBSD [25]) then we can perform re-projection and gain reasonable indexing success which is demonstrated with the example iron data set shown with this work. Perhaps more excitingly, it is likely that the spherical approach will prove useful when less conventional capture geometries are used, as the divergence of the Kossel cones is naturally encoded when the pattern is projected onto the sphere. For instance, it is well known that this divergence has caused significant problems when indexing transmission Kikuchi patterns when the pattern centre no longer located within the detector screen.

8. Conclusion

We have outlined and demonstrated methods to perform analysis of EBSD patterns in a spherical frame. We can summarise our conclusions as:

- We have converted a discrete description of the EBSD pattern, as projected on the a spherical pattern (the 'crystal ball'), into an approximation using spherical fast Fourier transforms.
- We can choose the appropriate bandwidth for this approximation to reduce the computation cost of describing the diffraction sphere and calculating with it.
- As the Fourier transform is closely related to the Radon transform, we can use the spherical FFT to create a spherical Radon transform, which transforms great circles into points on the sphere.
- The spherical Radon transform can be used to localise the bands within the diffraction pattern, and convolution with an 'average' band (similar to a butterfly mask) enables bands from multiple plane families to be localised.

- The spherical Radon transform can be used to extract band profiles, via an integration about great and small circles on the sphere, and this is likely useful for fine structure analysis.
- The spherical Radon transform can be applied to experimental patterns which contain an incomplete description of the diffraction pattern and subsequently indexed, with the orientation determined using AstroEBSD, with an ultimate precision of $< 0.1^\circ$.
- Cross correlation of an experimental pattern, projected on the sphere and then approximated, the master sphere is performed to precisely determine the crystal orientation. This spherical template matching method is robust and generates a precision of typically $< 0.1^\circ$.

9. Data Statement

The example iron data set can be found on Zenodo (<https://doi.org/10.5281/zenodo.1214828>). Upon article acceptance the full code for this manuscript will be released to Zenodo.

Acknowledgements

TBB acknowledges funding of his research fellowship from the Royal Academy of Engineering. We thank Alex Foden for useful discussions regarding pattern matching. We thank Jim Hickey for assisting with the example iron data set which was captured in the Harvey Flower EM suite at Imperial College on equipment supported by the Shell AIMS UTC. We thank Aimo Winkelmann for assistance with the spherical reprojection and dynamical pattern generation. Finally, we thank the anonymous reviewers for their valuable comments and suggestions.

References

[1] A. J. Wilkinson, T. B. Britton, Strains, planes, and ebsd in materials science, *Materials Today* 15 (9) (2012) 366–376. doi:Doi10.1016/S1369-7021(12)70163-3.
 URL <GotoISI>://WOS:000310422900015

[2] E. Rauch, J. Portillo, S. Nicolopoulos, D. Bultreys, S. Rouvimov, P. Moeck, Automated nanocrystal orientation and phase mapping in the transmission electron microscope on the basis of precession electron diffraction, *Zeitschrift für Kristallographie - Crystalline Materials* 225. doi:10.1524/zkri.2010.1205.
 URL <https://doi.org/10.1524/zkri.2010.1205>

[3] B. Adams, S. Wright, K. Kunze, Orientation imaging: The emergence of a new microscopy, *Metallurgical Transactions A* 24 (4) (1993) 819–831. doi:DOI10.1007/BF02656503.
 URL <https://link.springer.com/article/10.1007/BF02656503>

[4] A. Day, Spherical ebsd, *Journal of Microscopy* 409. doi:10.1111/j.1365-2818.2008.02011.x.

[5] Y. H. Chen, S. U. Park, D. Wei, G. Newstadt, M. A. Jackson, J. P. Simmons, M. De Graef, A. O. Hero, A dictionary approach to electron backscatter diffraction indexing, *Microsc Microanal* 21 (3) (2015) 739–52. doi:10.1017/S1431927615000756.
 URL <https://www.ncbi.nlm.nih.gov/pubmed/26055190>

[6] A. Winkelmann, C. Trager-Cowan, F. Sweeney, A. P. Day, P. Parbrook, Many-beam dynamical simulation of electron backscatter diffraction patterns, *Ultramicroscopy* 107 (4-5) (2007) 414–421. doi:10.1016/j.ultramic.2006.10.006.
 URL <GotoISI>://WOS:000244373700018

[7] N. Krieger Lassen, Automatic localisation of electron backscattering pattern bands from hough transform, *Materials Science and Technology* 12 (10) (1996) 837–843. doi:DOI10.1179/mst.1996.12.10.837.
 URL <https://doi.org/10.1179/mst.1996.12.10.837>

[8] A. Foden, D. Collins, A. Wilkinson, T. Britton, Indexing electron backscatter diffraction patterns with a refined template matching approach, ArXiv Preprint.
 URL <https://arxiv.org/abs/1807.11313>

[9] A. J. Wilkinson, D. M. Collins, Y. Zayachuk, R. Korla, A. Vilalta-Clemente, Applications of multivariate statistical methods and simulation libraries to analysis of electron

backscatter diffraction and transmission kikuchi diffraction datasets, ArXiv Preprint.

URL <https://arxiv.org/abs/1806.02087>

- [10] A. J. Wilkinson, G. Meaden, D. J. Dingley, High-resolution elastic strain measurement from electron backscatter diffraction patterns: New levels of sensitivity, *Ultramicroscopy* 106 (4-5) (2006) 307–313. doi:10.1016/j.ultramic.2005.10.001.
URL <GotoISI>://WOS:000236042300008
- [11] P. Anuta, Spatial registration of multispectral and multitemporal digital imagery using fast fourier transform techniques, *IEEE Transactions on Geoscience Electronics* 8 (4) (1970) 353–368. doi:10.1109/TGE.1970.271435.
- [12] E. W. Weisstein, Cross-correlation theorem, <http://mathworld.wolfram.com/Cross-CorrelationTheorem.html>, accessed: 2018-05-28.
- [13] S. Kunis, A note on stability results for scattered data interpolation on euclidean spheres, *Advances in Computational Mathematics* 30 (4) (2009) 303–314. doi:10.1007/s10444-008-9069-4.
URL <GotoISI>://WOS:000264513100001
- [14] S. Kunis, D. Potts, Fast spherical fourier algorithms, *Journal of Computational and Applied Mathematics* 161 (1) (2003) 75–98. doi:10.1016/S0377-0427(03)00546-6.
URL <GotoISI>://WOS:000186545000005
- [15] D. Potts, J. Prestin, A. Vollrath, A fast algorithm for non equispaced fourier transforms on the rotation group, *Numer. Algorithms* 52 (2009) 355–384.
- [16] R. Hielscher, D. Potts, J. Prestin, H. Schaeben, M. Schmalz, The radon transform on $so(3)$: a fourier slice theorem and numerical inversion, *Inverse Problems* 24 (2). doi:Artn0250110.1088/0266-5611/24/2/025011.
URL <GotoISI>://WOS:000254375500012
- [17] R. Hielscher, J. Prestin, A. Vollrath, Fast summation of functions on the rotation group, *Mathematical Geosciences* 42 (7) (2010) 773–794. doi:10.1007/s11004-010-9281-x.
URL <GotoISI>://WOS:000281859900004

[18] D. Mainprice, F. Bachmann, R. Hielscher, H. Schaeben, Descriptive tools for the analysis of texture projects with large datasets using mtex: strength, symmetry and components, Rock Deformation from Field, Experiments and Theory: A Volume in Honour of Ernie Rutter 409 (2015) 251–271. doi:10.1144/Sp409.8.
 URL <Go to ISI>://WOS:000367998600014

[19] D. Mainprice, F. Bachmann, R. Hielscher, H. Schaeben, G. E. Lloyd, Calculating anisotropic piezoelectric properties from texture data using the mtex open source package, Rock Deformation from Field, Experiments and Theory: A Volume in Honour of Ernie Rutter 409 (2015) 223–249. doi:10.1144/Sp409.2.
 URL <Go to ISI>://WOS:000367998600013

[20] M. Graf, Numerical spherical designs on s^2 .

[21] M. Graf, Quadrature rules on manifolds.

[22] J. Keiner, S. Kunis, D. Potts, Using nfft3 - a software library for various nonequispaced fast fourier transforms, ACM Trans. math. Software 36 (2009) 1–30.

[23] J. Keiner, S. Kunis, D. Potts, Efficient reconstruction of functions on the sphere from scattered data, Journal of Fourier Analysis and Applications 13 (4) (2007) 435–458. doi:10.1007/s00041-006-6915-y.
 URL <Go to ISI>://WOS:000248920200007

[24] C. Maurice, R. Fortunier, A 3d hough transform for indexing ebsd and kossel patterns, Journal of Microscopy 230 (3) (2008) 520–529. doi:DOI10.1111/j.1365-2818.2008.02045.x.
 URL <Go to ISI>://WOS:000256161300021

[25] T. Britton, V. Tong, J. Hickey, A. Foden, A. Wilkinson, Astroebsd: exploring new space in pattern indexing with methods launched from an astronomical approach, ArXiv Preprint.
 URL <https://arxiv.org/abs/1804.02602>

[26] P. T. Pinard, M. Lagacé, P. Hovington, D. Thibault, R. Gauvin, An open-source engine for the processing of electron backscatter patterns: Ebsd-image, Microscopy and Micro-

analysis 17 (2) (2011) 374–385. doi:DOI10.1017/S1431927611000456.
URL <https://doi.org/10.1017/S1431927611000456>

[27] A. Morawiec, Determination of orientations from monochromatic diffraction patterns as the constellation problem, IOP Conference Series: Materials Science and Engineering 82 (1) (2015) 012008.
URL <http://stacks.iop.org/1757-899X/82/i=1/a=012008>

[28] J. Bassinger, D. Fullwood, J. Kacher, B. Adams, Pattern center determination in electron backscatter diffraction microscopy, Microscopy and Microanalysis 17. doi:10.1017/S1431927611000389.
URL <https://www.cambridge.org/core/journals/microscopy-and-microanalysis/article/pattern-center-determination-in-electron-backscatter-diffraction-microscopy/782ECC7897206E98B86870C1F2EAB780>

[29] A. Winkelmann, G. Nolze, M. Vos, F. Salvat-Pujol, W. Werner, Physics-based simulation models for ebsd: advances and challenges, IOP Conference Series: Materials Science and Engineering 109. doi:10.1088/1757-899X/109/1/012018.
URL <http://iopscience.iop.org/article/10.1088/1757-899X/109/1/012018/pdf>

[30] A. Winkelmann, Dynamical effects of anisotropic inelastic scattering in electron backscatter diffraction, Ultramicroscopy doi:10.1016/j.ultramic.2008.05.002.